Effect of Parameter Variations on the Hemodynamic Response Under Rotary Blood Pump Assistance

*Einly Lim, †Socrates Dokos, ‡Robert F. Salamonsen, ‡Franklin L. Rosenfeldt, †Peter J. Ayre, and †Nigel H. Lovell

*Department of Biomedical Engineering, Faculty of Engineering, University of Malaya, Kuala Lumpur, Malaysia; †Graduate School of Biomedical Engineering, University of New South Wales, Sydney, Australia; and ‡Department of Surgery, Alfred Hospital, Melbourne, Australia

Abstract: Numerical models, able to simulate the response of the human cardiovascular system (CVS) in the presence of an implantable rotary blood pump (IRBP), have been widely used as a predictive tool to investigate the interaction between the CVS and the IRBP under various operating conditions. The present study investigates the effect of alterations in the model parameter values, that is, cardiac contractility, systemic vascular resistance, and total blood volume on the efficiency of rotary pump assistance, using an optimized dynamic heart–pump interaction model previously developed in our laboratory based on animal experimental measurements obtained from five canines. The effect of mean pump speed and the circulatory perturbations on left and right ventricular pressure volume loops, mean aortic pressure, mean cardiac output, pump assistance ratio, and pump flow pulsatility from both the greyhound experiments and model simulations are demonstrated. Furthermore, the applicability of some of the previously proposed control parameters, that is, pulsatility index (PI), gradient of PI with respect to pump speed, pump differential pressure, and aortic pressure are discussed based on our observations from experimental and simulation results. It was found that previously proposed control strategies were not able to perform well under highly varying circulatory conditions. Among these, control algorithms which rely on the left ventricular filling pressure appear to be the most robust as they emulate the Frank–Starling mechanism of the heart. **Key Words:** Heart–pump interaction model—Implantable rotary blood pump—Heart failure—Ventricular assist devices.

Congestive heart failure (CHF) is a serious health condition characterized by the inability of the heart to supply adequate blood flow and therefore oxygen delivery to tissues and organs in the body. Advancement in the field of cardiac assist device technology has resulted in implantable rotary blood pumps (IRBPs) becoming widely used in these patients. Furthermore, with evidence showing successful experience for prolonged periods of implantation in patients, IRBPs have moved from bridge-to-transplant to bridge-to-recovery or permanent support for chronic heart failure patients (1). In a

long-term unsupervised environment, as patients go through different activity levels from sleep to exercise, underpumping or overpumping may occur, leading to unacceptable risks such as collapse of the left ventricle or impairment of the right heart function (2). For example, some patients implanted with IRBPs have reported feeling faint during postural changes, Valsalva maneuvers, coughing, or straining. This is further complicated by the insensitivity of IRBPs to preload (3) and the remaining intrinsic ventricular function.

Numerical models (4–7), in vitro mock circulatory experiments (8–10), in vivo animal studies (11–13), as well as human trials (14–16) have been widely used to study the interaction between the IRBPs and the cardiovascular system (CVS). McConnell et al. (11) evaluated load-dependent ventricular function during left ventricular assist device (LVAD) support based on telemetered measurements of left ventricular (LV) pressure in six adult

sheep. In another study, Chiang et al. (12) investigated the cardiovascular and metabolic responses in calves implanted with an AbioCor artificial heart during treadmill exercise. To determine the optimal support level of an LVAD, Goldstein et al. (13) measured the LV myocardial oxygen consumption as well as stroke work in an ovine model of microinfarction-induced CHF under different pump assistance levels. Although in vivo animal studies have been very useful in the study of heart–pump interaction, they are inconclusive at present due to limitations in animal models of heart failure and complexity of the experimental procedures (5).

On the contrary, numerical models, able to simulate the response of the human CVS in the presence of an IRBP, can provide additional insights into the dynamics of the assisted circulation and address research questions not easily answered in vivo. In particular, hemodynamic response to circulatory perturbations, such as cardiac contractility, ventricular preload, and afterload, which may endanger patients, can be investigated individually using a numerical model. Numerical models also offer an excellent platform for the development and evaluation of robust physiological pump control algorithms by easily allowing reproducible numerical experiments under identical conditions. For example, Arndt et al. (17) have reported a dependency of the pulsatility index (PI) on heart contractility, afterload, and preload.

Therefore, the aim of the present article is to study the effect of alterations in the model parameter values, that is, cardiac contractility, systemic vascular resistance (SVR), and total blood volume (V_{total}) on the efficiency of LVAD support using a centrifugal blood pump, based on the optimized dynamic heart–pump interaction model previously developed in our laboratory. Using our observations from both animal experimental and simulation results, we comparatively evaluate a number of previously proposed control parameters, including PI control (15,18,19), gradient of PI with respect to pump speed (GPI) control (17), constant average pressure difference control (20–22), and constant aortic pressure control (7).

METHODS

Optimized heart–pump interaction model

A dynamic heart–pump interaction model has been developed based on experimental measurements obtained from five canines (greyhounds)

implanted with an IRBP, over a wide range of operating conditions (23). The model included descriptions of the left and right heart, the systemic and pulmonary circulations, as well as the IRBP. In addition, it also takes into account various model features which provide important insights into the dynamics of heart–pump interaction, such as the curvilinearity of the end-systolic pressure volume relationship (ESPVR), direct ventricular interaction through the septum and pericardium, the nonlinear pressure volume relationship in the aorta and the vena cava compartment, the nonlinear pulmonary peripheral resistance, the suction resistance used to describe the collapse of the ventricle during a suction event (24), as well as the influence of the pump inflow and outflow cannulae.

Five canine experiments were performed to investigate heart–pump interaction over a wide range of operating conditions, including variations in (i) cardiac contractility and heart rate by administration of a beta-blocker (Metoprolol); (ii) SVR (or afterload) by administration of Metaraminol or sodium nitroprusside; and (iii) V_{total} (or preload) by varying the rate of suction from a cardiotomy machine. The LVAD used during the experiments is the VentrAssist (25), a fully implantable centrifugal rotary blood pump system. Each animal experiment consisted of seven speed ramp tests, that is, the control state ("healthy condition," $H1$) and the reduced cardiac contractility states which included the three different afterload conditions (afterload low, $H2$; afterload medium, $H3$; and afterload high, $H4$) and the three different preload conditions (preload low, $H5$; preload medium, $H6$; and preload high, $H7$). Parameters of the heart–pump interaction model were optimized for each animal to reproduce individual experimental datasets in a quantitative sense. Eleven parameters related to LV and right ventricular (RV) contractilities ($V_{d,lvf}$, α_{lvf}, β_{lvf}, $V_{d,rvf}$, α_{rvf}, and β_{rvf}), systemic and pulmonary peripheral resistances (R_{sa}, A_{pa}, B_{pa}, and C_{pa}), as well as systemic vein unstressed volume ($V_{0,sv}$) were individually estimated in $H1$ to $H5$ to simulate the effect of Metoprolol or Metaraminol. The remaining parameter, that is, total V_{total}, was assumed to be shared by all these five conditions. On the contrary, $H5$, $H6$, and $H7$ were assumed to share the same values for all parameters except V_{total}. Simulated responses of the model were shown to agree well with the experimental data, both in terms of mean values and response dynamics. A detailed description of the model as well as parameter values for each canine (greyhound 1–5) under different conditions ($H1$–$H7$) can be obtained from (23).

Parameter variation studies

Effect of ventricular contractility

To investigate the effect of LV and RV contractility on the efficiency of rotary pump assistance, we performed simulations using the optimized model parameters for greyhound 2 for the healthy condition ($H1$) as baseline values. Different combinations of parameter values which describe the LV and RV ESPVR (α_{lvf}, β_{lvf}, $V_{d,lvf}$, α_{rvf}, β_{rvf}, and $V_{d,rvf}$) were chosen from the optimized results for the same greyhound under other conditions to represent different cardiac contractility states: (i) optimized LV and RV ESPVR parameters from $H1$ were used to represent healthy condition, Cn; (ii) optimized LV and RV ESPVR parameters from $H3$ were used to simulate depressed LV and RV contractility, Clr; (iii) optimized LV ESPVR parameters from $H3$ and RV ESPVR parameters from $H1$ were used to represent reduced LV contractility, Cl; and (iv) optimized LV ESPVR parameters from $H1$ and RV ESPVR parameters from $H3$ were used to simulate depressed RV contractility, Cr.

Effect of R_{sa}

To illustrate the individual effect of R_{sa} on heart–pump interaction, we performed simulations using the optimized model parameters for greyhound 4 under the "afterload medium condition" ($H3$) as baseline values. Different values for R_{sa} were chosen to represent different systemic afterload conditions:

(i) afterload low ($R_{sa} = 0.35$ mm Hg.s/mL), Rl; (ii) afterload medium ($R_{sa} = 0.64$ mm Hg.s/mL, i.e., optimized value for $H3$ condition), Rm; and (iii) afterload high ($R_{sa} = 1.50$ mm Hg.s/mL), Rh.

Effect of V_{total}

To illustrate the individual effect of V_{total} on the efficiency of rotary pump assistance, we performed simulations using the optimized model parameters for greyhound 5 under "volume low condition" ($H5$) as baseline values. Different values for V_{total} were chosen to represent varying levels of V_{total}: (i) volume low ($V_{total} = 2864$ mL, i.e., optimized value for $H5$ condition), Vl; (ii) volume medium ($V_{total} = 3400$ mL, i.e., optimized value for $H6$ condition), Vm; (iii) volume high ($V_{total} = 3952$ mL, i.e., optimized value for $H7$ condition), Vh; and (iv) volume high (extreme) ($V_{total} = 5452$ mL, i.e., optimized value for $H7$ condition + 1500 mL), VH.

RESULTS

Effect of ventricular contractility

As demonstrated in Fig. 1, reduced LV and RV contractilities (Clr) produced a rightward shift of the pressure volume loops, resulting in increased LV and RV end-diastolic volumes, end-systolic volumes, and end-diastolic pressures, thus significantly increasing the ventricular wall stress. Peak systolic LV and RV pressure as well as stroke volume (SV) was
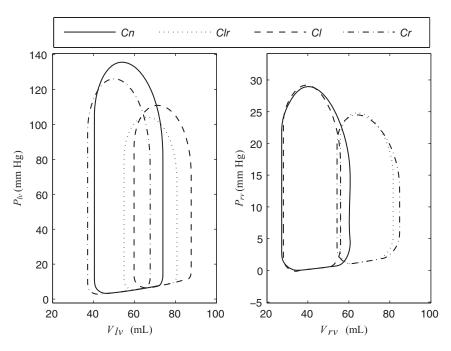

FIG. 1. Effect of heart contractility on the LV and RV pressure volume loops during pump occlusion from the model simulations using optimized model parameters for greyhound 2 under healthy condition ($H1$) as baseline values. During pump occlusion, the pump outflow cannula was occluded to record the baseline hemodynamic variables. Cn, model simulations using optimized LV and RV ESPVR parameters from $H1$ to represent a healthy condition; Clr, model simulations using optimized LV and RV ESPVR parameters from $H3$ to simulate depressed LV and RV contractility; Cl, model simulations using optimized LV ESPVR parameters from $H3$ and RV ESPVR parameters from $H1$ to represent reduced LV contractility; Cr, model simulations using optimized LV ESPVR parameters from $H1$ and RV ESPVR parameters from $H3$ to simulate depressed RV contractility.
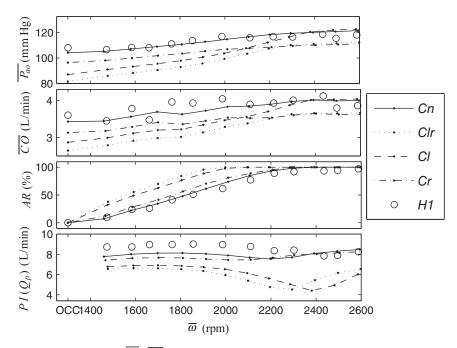
FIG. 2. Effect of $\bar{\omega}$ and heart contractility on $\overline{P_{ao}}$, $\overline{CO}$, AR, and $PI(Q_p)$ from both the greyhound experiment and model simulations using optimized model parameters for greyhound 2 under healthy condition (*H*1) as baseline values. OCC, pump occlusion, where the pump outflow cannula was occluded to record the baseline hemodynamic variables; *Cn*, model simulations using optimized LV and RV ESPVR parameters from *H*1 to represent healthy condition (suction occurring at $\bar{\omega}$ = 2200 rpm); *Clr*, model simulations using optimized LV and RV ESPVR parameters from *H*3 to simulate depressed LV and RV contractilities (suction occurring at $\bar{\omega}$ = 2300 rpm); *Cl*, model simulations using optimized LV ESPVR parameters from *H*3 and RV ESPVR parameters from *H*1 to represent reduced LV contractility (suction occurring at $\bar{\omega}$ = 2400 rpm); *Cr*, model simulations using optimized LV ESPVR parameters from *H*1 and RV ESPVR parameters from *H*3 to simulate depressed RV contractility (suction occurring at $\bar{\omega}$ = 2000 rpm); *H*1, experimental measurements from greyhound 2 under healthy condition (suction occurring at $\bar{\omega}$ = 2200 rpm).

decreased. Reduced LV contractility alone (*Cl*) produced the same directional change in the LV pressure volume loop, but with decreased RV end-diastolic volume (or preload to the right ventricle). On the contrary, depressed RV contractility alone (*Cr*) caused a rightward shift of the RV pressure volume loop, with decreased LV end-diastolic volume (or preload to the left ventricle).

To illustrate the trend of hemodynamic and pump variables with increasing mean pump speed ($\bar{\omega}$) under varying LV and RV contractilities, mean values of key variables from the experiment (greyhound 2 under healthy condition) and/or model were plotted in Fig. 2. Under 0% pump support (baseline condition), normal LV and RV contractility conditions (*H*1 and *Cn*) yielded the highest mean aortic pressure ($\overline{P_{ao}}$) and mean cardiac output ($\overline{CO}$), followed by depressed RV contractility (*Cr*), depressed LV contractility (*Cl*), and depressed LV/RV contractility (*Clr*) conditions.

During pump assist, most variables showed a change in trend (or slope) with respect to $\bar{\omega}$ at "knee points" corresponding to the transition between ventricular ejection (*VE*) (i.e., when aortic valve flow,

$Q_{av} > 0$) and aortic valve nonopening (*ANO*) (i.e., when $Q_{av} = 0$), and between *ANO* and ventricular suction states. Compared to simulations using healthy LV ESPVR parameters (*Cn* and *Cr*), increasing $\bar{\omega}$ produced a higher increase in $\overline{P_{ao}}$ and $\overline{CO}$ under depressed LV contractility conditions (*Clr* and *Cl*). Simulations using the same RV contractility parameters (*Cn* vs. *Cl* and *Clr* vs. *Cr*) produced comparable maximum achievable $\overline{CO}$, indicating the importance of RV contractility in determining the efficiency of pump assistance. In addition, at low $\bar{\omega}$, mean pump flow (Q_p) was higher with depressed LV contractility (*Clr* and *Cl*) due to lower differential pressure across the pump, producing a higher pump assistance ratio (*AR*) and an earlier transition into *ANO* state. *AR* is defined as Q_p divided by $\overline{CO}$, multiplied by 100% to get the percentage value. In both experiments and simulations under normal cardiac contractility conditions (*H*1 and *Cn*) with high *SV* and low LV end-systolic volume (V_{lves}), suction occurred temporarily within each heart beat before full LV decompression, and this avoids further increases in $\overline{P_{ao}}$ and $\overline{CO}$.

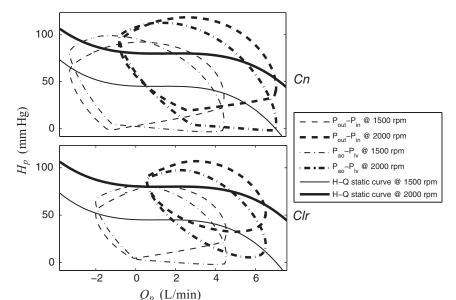In regard to pump flow, speed, and current pulsatility ($PI(Q_p)$, $PI(\omega)$, and $PI(I)$), defined as their cor-

FIG. 3. Effect of $\bar{\omega}$ and heart contractility on pump pressure flow loops from the model simulations using optimized model parameters for greyhound 2 under healthy condition (H1) as baseline values. H_p, pump differential pressure; Q_p, pump flow; Cn, model simulations using optimized LV and RV ESPVR parameters from H1 to represent healthy condition; Clr, model simulations using optimized LV and RV ESPVR parameters from H3 to simulate depressed LV and RV contractilities.

responding amplitudes, simulations with reduced LV contractility (Clr and Cl) demonstrated a gradual decrease in $PI(Q_p)$ until the point of suction. On the contrary, as suction occurred before full LV decompression in the other two conditions (Cn and Cr), we did not observe any significant decrease in $PI(Q_p)$ throughout the whole range of pumping speeds. The relationship between $PI(\omega)/PI(I)$ and $\bar{\omega}$ followed a similar trend with $PI(Q_p)$, except at the region of regurgitant pump flow where it increased with increasing $\bar{\omega}$.

To illustrate the pressure flow characteristics of the rotary blood pump under healthy and reduced heart contractility conditions, we plotted the pressure flow loops in Fig. 3 for two different $\bar{\omega}$. Compared to the healthy condition (Cn), reduced LV and RV contractilities (Clr) decreased the area of the pressure flow loops due to the lesser contribution from the native heart. Pressure across the pump ($P_{out} - P_{in}$) was higher than the pressure difference between the left ventricle and the aorta ($P_{ao} - P_{lv}$) during end systole, due to pressure loss in the cannula.

Effect of systemic afterload

Figure 4 shows that increasing R_{sa} substantially increases peak LV systolic pressure (i.e., afterload "seen" by the left ventricle), thereby increasing LV end-diastolic volume (V_{lved}) and V_{lves}, leading to a decrease in SV. Increasing V_{lved} and left atrial pressure (P_{la}) leads to an increase in pulmonary arterial pressure (P_{pa}) and peak RV systolic pressure, that is, afterload seen by the right ventricle. On the contrary,
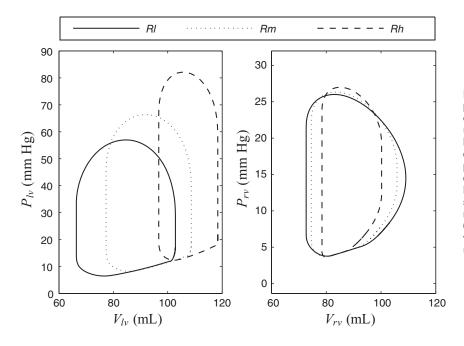
preload to the right ventricle decreases due to a reduction in venous return.

Figure 5 summarizes the effect of R_{sa} and $\bar{\omega}$ on the hemodynamic and pump variables from both experiment (greyhound 4 under H3 condition) and/or model. Under 0% pump support (baseline condition), increasing R_{sa} increases $\overline{P_{ao}}$ while reducing SV, leading to a decrease in $\overline{CO}$.

During pump assist, the rate of increase in $\overline{P_{ao}}$ and $\overline{CO}$ with increasing $\bar{\omega}$ was not significantly varied by R_{sa} under the VE state. Compared to the VE state, the rate of change of the above variables with increasing $\bar{\omega}$ increased during the ANO state. In terms of AR, decreasing R_{sa} increases AR due to a decrease in the pump differential pressure. In regard to $\overline{Q_p}$ and PI, the change in trend of $PI(Q_p)$, $PI(\omega)$, and $PI(I)$ with increasing $\bar{\omega}$ across various pumping state transitions was similar to that described in the section "Effect of ventricular contractility."

To illustrate the pressure flow characteristics of the rotary blood pump under different systemic afterload conditions, we plotted the pressure flow loops in Fig. 6 at two different $\bar{\omega}$. Increasing R_{sa} shifted the pressure-flow loops leftward while increasing the area of the loop. Due to increasing pressure loss across the cannula with increasing pump flow, there was a huge difference (~55 mm Hg) between the pressure difference across the pump during end systole ($P_{out} - P_{in}$) and that seen by the circulation (between the left ventricle and the aorta, i.e., $P_{ao} - P_{lv}$) at lower R_{sa} and higher $\bar{\omega}$ conditions.
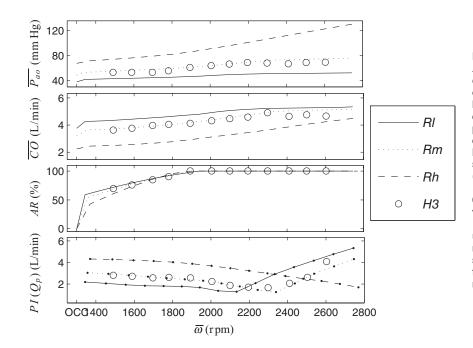
FIG. 4. Effect of SVR on the LV and RV pressure volume loops during pump occlusion from the model simulations using optimized parameters for greyhound 4 under the "afterload medium condition" (*H*3) as baseline values. During pump occlusion, the pump outflow cannula was occluded to record the baseline hemodynamic variables. *Rl*, model simulations using $R_{sa} = 0.35$ mm Hg.s/mL; *Rm*, model simulations using $R_{sa} = 0.64$ mm Hg.s/mL (i.e., optimized R_{sa} value for *H*3); *Rh*, model simulations using $R_{sa} = 1.5$ mm Hg.s/mL.
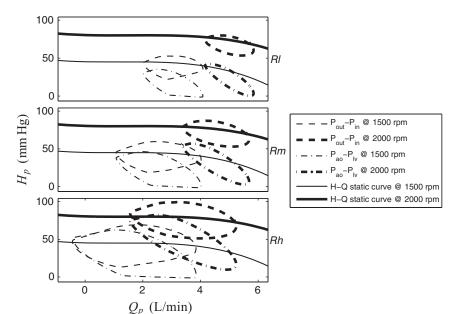
Effect of preload

Figure 7 shows that increasing V_{total} produces a rightward shift of the pressure volume loops, causing an increase in both LV and RV end-diastolic volume, end-systolic pressure, and *SV*. At very high V_{total} (*VH*), a significant increase in P_{la} substantially increased afterload seen by the right ventricle, leading to a much larger increase in RV end-diastolic volume compared to LV end-diastolic volume. However, at this stage, there was no further increase

in *SV* as the heart was already operating at the higher end of the Frank–Starling curve.

To illustrate the trend of hemodynamic and pump variables with increasing $\bar{\omega}$ under varying V_{total} conditions, mean values of key variables from the experiment (greyhound 3 under *H*5 and *H*7 conditions) and/or model were plotted in Fig. 8. Under 0% pump support (baseline condition), increasing V_{total} increased all pressures, flows, and volumes in the CVS. With increasing $\bar{\omega}$, $\overline{Q_p}$ increased in all conditions,

FIG. 5. Effect of $\bar{\omega}$ and R_{sa} on $\overline{P_{ao}}$, $\overline{CO}$, *AR*, and *PI*(Q_p) from both the greyhound experiment and model simulations using optimized model parameters for greyhound 4 under the "afterload medium condition" (*H*3) as baseline values. OCC, pump occlusion, where the pump outflow cannula was occluded to record the baseline hemodynamic variables; *Rl*, model simulations using $R_{sa} = 0.35$ mm Hg.s/mL (suction occurring at $\bar{\omega} = 2100$ rpm); *Rm*, model simulations using $R_{sa} = 0.64$ mm Hg.s/mL (i.e., optimized R_{sa} value for *H*3) (suction occurring at $\bar{\omega} = 2350$ rpm); *Rh*, model simulations using $R_{sa} = 1.5$ mm Hg.s/mL (suction has not occurred throughout the speed ramp study); *H*3, experimental measurements from greyhound 4 under "afterload medium condition" (suction occurring at $\bar{\omega} = 2300$ rpm).
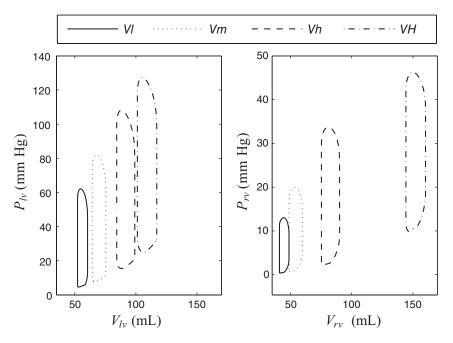
FIG. 6. Effect of $\bar{\omega}$ and R_{sa} on pump pressure flow loops from the model simulations using optimized parameters for greyhound 4 under "afterload medium condition" (*H*3) as baseline values. H_p, pump differential pressure; Q_p, pump flow; *Rl*, model simulations using $R_{sa} = 0.35$ mm Hg.s/mL; *Rm*, model simulations using $R_{sa} = 0.64$ mm Hg.s/mL (i.e., optimized R_{sa} value for *H*3); *Rh*, model simulations using $R_{sa} = 1.5$ mm Hg.s/mL.

counteracted by a slower decrease in mean aortic valve flow ($\overline{Q_{av}}$), leading to an overall increase in $\overline{CO}$. In contrast, maximum achievable $\overline{Q_p}$ and $\overline{CO}$ increased with increasing V_{total}. However, due to substantial increases in RV afterload and preload at excessively high V_{total} conditions (*VH*), the right ventricle was not able to efficiently utilize the Frank–Starling mechanism to generate further increases in *SV*. As a result, there was no further improvement at this stage despite an increase in pressure, volume, and stroke work, which imposed increasing oxygen demand on the heart. In terms of *AR*, increasing V_{total} led to an increase in $\overline{CO}$ through greater contributions from the native heart rather than the assist device. Consequently, the *AR* was lower at higher V_{total}.

However, increasing V_{total} caused an increase in the pressure flow loop area (Fig. 9) due to increasing contribution from the native heart. High regurgitant pump flow can be observed at low pump speed settings, particularly under high V_{total}.

FIG. 7. Effect of V_{total} on the LV and RV pressure volume loops during pump occlusion from the model simulations using optimized parameters for greyhound 3 under "volume low condition" (*H*5) as baseline values. During pump occlusion, the pump outflow cannula was occluded to record the baseline hemodynamic variables. *Vl*, model simulations using $V_{total} = 2864$ mL (i.e., optimized V_{total} value for *H*5); *Vm*, model simulations using $V_{total} = 3400$ mL (i.e., optimized V_{total} value for *H*6); *Vh*, model simulations using $V_{total} = 3952$ mL (i.e., optimized V_{total} value for *H*7); *VH*, model simulations using $V_{total} = 5452$ mL (i.e., optimized V_{total} value for *H*7 + 1500 mL).
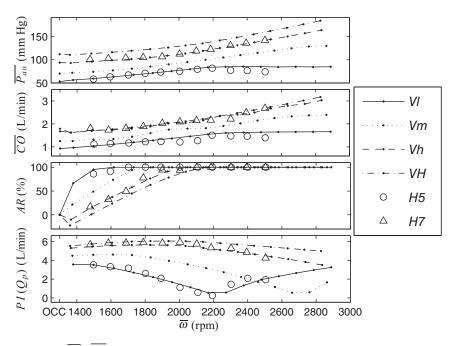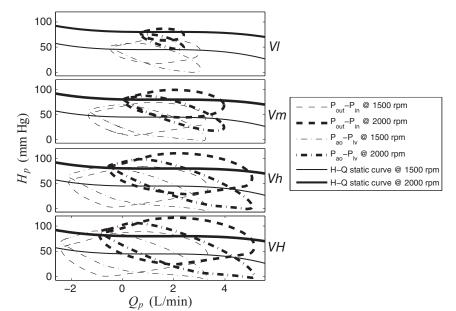
FIG. 8. Effect of $\bar{\omega}$ and V_{total} on $\overline{P_{ao}}$, $\overline{CO}$, AR, and $PI(Q_p)$ from both the greyhound experiment and model simulations using optimized model parameters for greyhound 3 under "volume low condition" (H5) as baseline values. OCC, pump occlusion, where the pump outflow cannula was occluded to record the baseline hemodynamic variables; Vl, model simulations using $V_{total} = 2864$ mL (i.e., optimized V_{total} value for H5) (suction occurring at $\bar{\omega} = 2200$ rpm); Vm, model simulations using $V_{total} = 3400$ mL (i.e., optimized V_{total} value for H6) (suction occurring at $\bar{\omega} = 2650$ rpm); Vh, model simulations using $V_{total} = 3952$ mL (i.e., optimized V_{total} value for H7) (suction has not occurred throughout the speed ramp study); VH, model simulations using $V_{total} = 5452$ mL (i.e., optimized V_{total} value for H7 + 1500 mL) (suction has not occurred throughout the speed ramp study); H5, experimental measurements from greyhound 3 under "volume low condition" (suction occurring at $\omega = 2200$ rpm); H7, experimental measurements from greyhound 3 under "volume high condition" (suction has not occurred throughout the speed ramp study).

DISCUSSION

In the present article, we have performed parameter variations on a validated heart–pump interaction model (23) to extend our understanding of the interactions between the CVS and the IRBP beyond what is readily available experimentally. In terms of pump speed variations in both experiments and model

FIG. 9. Effect of $\bar{\omega}$ and V_{total} on pump pressure flow loops from the model simulations using optimized parameters for greyhound 3 under "volume low condition" (H5) as baseline values. H_p: pump differential pressure; Q_p: pump flow. Vl: Model simulations using $V_{total} = 2864$ mL (i.e., optimized V_{total} value for H5); Vm: Model simulations using $V_{total} = 3400$ mL (i.e., optimized V_{total} value for H6); Vh: Model simulations using $V_{total} = 3952$ mL (i.e., optimized V_{total} value for H7); VH: Model simulations using $V_{total} = 5452$ mL (i.e., optimized V_{total} value for H7 + 1500 mL).

simulations, we covered a wide range of pump speed settings (from 1250 to 3000 rpm). This more than covers the range of pump speed variations possibly occurring in a clinical setting. In terms of cardiac contractility, SVR, and total blood volume, different perturbations were carried out during the experiments and in the model to perturb the system far away from the normal operating point (which we believe are able to cover the wide physiological ranges possible in patients but not easily reproducible in acute animal heart failure models). For example, the range of SVR in our experimental and simulation results is between 0.45 and 1.6 mm Hg.s/mL, while the anticipated ranges in human are between 0.54 and 1.2 mm Hg.s/mL (26). Experimentally, it is only possible to perform a limited range/number of parameter variations due to inadequate animal models of heart failure, difficulties in altering and controlling certain CVS variables in the animal preparations, and/or the likelihood of sacrificing the animal.

Effect of cardiac contractility, afterload, and preload on heart–pump interaction

There has been considerable debate regarding whether it is more beneficial to operate an LVAD under partial assistance ($AR < 100\%$) or full assistance (i.e., $AR = 100\%$) (13,27,28). Goldstein et al. (13) suggested that partial LVAD support significantly reduced LV myocardial oxygen consumption in a failing heart, while full assist may result in undesirable effects such as aortic valve stasis, myocardial atrophy, and the impairment of RV function. As transition into the *ANO* state occurred at much lower pump speeds under more severe LV contractility conditions (as shown in our results), full assist is normally required in these patients to achieve sufficient flow. Furthermore, both our experimental measurements and model simulations showed that the ability of the LVAD in improving $\overline{CO}$ was highest under the depressed LV contractility conditions (Fig. 2). The results were consistent with published experimental findings (28,29). Therefore, it can be concluded that full assist is beneficial under more severe LV failing conditions with high end-diastolic volume, while partial assist is more suitable in the recovering ventricle. The difference in LVAD efficiency between healthy and depressed cardiac contractility could be explained by Guyton (30), who suggested that under normal resting conditions, $\overline{CO}$ is controlled almost entirely by peripheral factors governing return of blood to the heart, while the heart controls the "permissible" amount of output that can be pumped. One observation from our experimental measurements is

that during speed ramp studies under healthy LV conditions, LV suction occurred temporarily during end systole at pump speeds before full LV decompression (or *ANO* state), that is, when maximum LV pressure ($P_{lv,max}$) was still relatively high. This is because at relatively high cardiac contractility, the left ventricle ejects a large amount of blood during systole, leading to low LV end-systolic volumes.

Our simulation results also showed that one important determinant of the maximum achievable $\overline{CO}$ under LVAD assistance is the RV contractility. As suggested by Farrar (31), the first basic principle of CVS–LVAD interaction which relates to RV function is that there is increased venous return to and $\overline{CO}$ from the right ventricle. Suction occurred when there was a mismatch between RV and LV output, that is, when the LVAD attempted to increase blood flow beyond the capability of the right ventricle. It was reported that right-sided circulatory failure (RSCF) occurs in 15–30% of the patients supported with an LVAD (32) due to three reasons: existing RSCF, reduced RV contractility due to leftward shift of the interventricular septum, and functional mismatch between the LVAD and the native circulation (31). Due to high sensitivity of the right ventricle to afterload, pulmonary afterload also played an important role in determining the efficiency of rotary pump support. LVAD assistance is most beneficial under normal pulmonary vascular resistance with passively elevated P_{pa}, as pump assistance is able to reverse pulmonary hypertension by reducing LV filling pressure (31).

In regard to the effect of afterload on the hemodynamic variables during LVAD assistance, our results showed that the best pumping speed for rotary blood pump operation varies substantially with SVR (systemic afterload) (Fig. 5). Due to high sensitivity of the rotary pump flow to pump differential pressure (33), an increase in $\overline{CO}$ with decreasing SVR was contributed mostly by the assist device rather than the native heart. The increase in Q_p due to a decrease in pump differential pressure significantly decreased LV end-diastolic volume, leading to a decrease in LV pumping efficiency through the Frank–Starling mechanism. The level of P_{ao} and $\overline{CO}$ increase with increasing pump speed is also relatively lower for low SVR conditions. Therefore, it may be more advantageous to drive the rotary blood pump at lower pump speeds under low SVR conditions, as there is an increased risk of suction associated with high pump speeds. On the contrary, regurgitant pump flow, which increases volume loading on the left ventricle, can be observed at high afterload pressures for lower pump speeds (34). As reported in the literature (35) and

shown in our results, suction occurred at higher pump speeds under higher SVR conditions due to an increase in the LV end-systolic volume with increasing SVR. Thus, it is more beneficial to operate an LVAD at higher speeds with increasing systemic afterload in order to more efficiently improve $\overline{CO}$ and LV unloading as well as avoid regurgitant pump flow, thereby reducing RV afterload (through a reduction in P_{la}) and myocardial oxygen consumption. However, care has to be taken to ensure that the arterial pressure is within physiologically reasonable limits in order to avoid overperfusion.

Increasing V_{total} increases $\overline{P_{ao}}$ and $\overline{CO}$ (Fig. 8), at the expense of increasing volume loading on the heart. However, it was observed from both our experimental data and model simulation results that excessively increasing V_{total} leads to pulmonary congestion with no further increase in SV, as the heart is already operating on the higher end of the Frank–Starling curve and therefore could not efficiently utilize the Frank–Starling mechanism. This phenomenon is frequently observed in heart failure patients with significant fluid retention (36). Although LVAD assistance substantially reduces pulmonary congestion by decreasing $\overline{P_{la}}$, the efficiency of the LVAD at high volume depends on the existing RV condition (32). We also observed an increase in pulmonary vascular resistance under low V_{total}, low SVR, and high pump speed conditions. One common feature shared by these three conditions is low $\overline{P_{la}}$ (below a threshold value of ~6 mm Hg), which reflected low pulmonary blood volume. An increase in pulmonary vascular resistance limits venous return to the left ventricle while increasing pulmonary afterload, leading to an earlier transition into suction (37). Consequently, there is a relatively lower augmentation of $\overline{CO}$ with increasing $\bar{\omega}$ under these conditions.

Comparison of existing control strategies

Due to the overall insensitivity of the rotary pump to preload, various physiological control strategies which attempt to adapt to varying cardiac demand and clinical states of the heart have been proposed. Three main criteria have been suggested for safe operation of an IRBP (38), including (i) sufficient $\overline{CO}$ to meet metabolic requirements; (ii) maintaining systolic arterial pressure within a physiological range to avoid overperfusion or underperfusion; and (iii) maintaining P_{la} within a normal physiological range to avoid pulmonary congestion and suction.

Among the various physiological control algorithms, preload-based control strategies are the most widely used for clinically available pumps, where the pump speed is adjusted according to the amount of venous return. The direct method of measuring preload to the ventricle is by using an implantable pressure sensor at the left atrium, ventricle, or pump inlet (39). However, due to reduction in system reliability, increased cost, and risks associated with the implantation of invasive sensors, researchers have looked into ways to indirectly estimate preload (15,17–19,40).

One of the most popular noninvasive preload-based control strategies is PI control, based on the close relationship between pump flow or differential pressure pulsatility and LV filling pressure (18). It was shown from the published findings as well as our experimental and model simulations that $PI(Q_p)$ decreases with increasing pump speed until the point of suction, and their relationship varies with heart contractility, afterload, and preload. Our simulation results (Figs. 2, 5, and 8) showed that $PI(Q_p)$ reaches its minimum value just before the onset of suction, and that this occurs at higher pump speeds with increasing SVR, cardiac contractility, and V_{total}. Furthermore, the magnitude of minimum $PI(Q_p)$ showed a substantial increase with increasing cardiac contractility, but remained relatively constant regardless of variations in SVR and V_{total}. The nonmonotonic function of $PI(Q_p)$ with respect to pump speed, with an abrupt change in slope when suction occurs, creates instability in classical feedback control, where the controller would react to an increase in $PI(Q_p)$ during suction by increasing pump speed even further. This has deleterious effects on the patients and therefore must be avoided. Inclusion of a suction detector (41) would effectively make the controller robust toward this discontinuity.

As reported by Arndt et al. (17), due to the dependence of PI on heart contractility, afterload, and preload, controlling PI to a fixed set point may fail to avoid adverse pumping states such as suction during sudden perturbations of the circulatory system. In order to overcome this problem, Arndt et al. proposed an extremum seeking algorithm which regulated the GPI. The clinician was allowed to choose either full assist before suction (minimum GPI), or at the boundary between partial assist and full assist (GPI = a predefined small value.). Some limitations of the control method included the risk of overperfusion and the difficulty in choosing the appropriate reference value for GPI. Although the changes in $PI(\omega)$ or $PI(I)$ showed a close resemblance with $PI(Q_p)$ during variations in $\bar{\omega}$, heart contractility,

SVR, and V_{total}, they showed a different trend under regurgitant flow in our experimental and simulation results (not shown), that is, an increase instead of a decrease with increasing $\bar{\omega}$. Therefore, compared to pump flow, they are less suitable as control parameters for PI control.

However, Giridharan et al. (20) proposed that maintaining a constant average pressure difference between the left ventricle and the aorta provided sufficient physiological perfusion to the body over a wide range of physical activities and clinical cardiac conditions. Furthermore, they developed a model-based method for the estimation of pump differential pressure using pump speed and current. Nevertheless, the present study uses a centrifugal blood pump which is less appropriate for use in model-based differential pressure estimation based on noninvasive pump parameters, due to the higher degree of decoupling between pump flow and pump differential pressure (20). Furthermore, it was shown from both our experiments and simulations (Figs. 3, 6, and 9) that although pressure across the pump ($P_{out} - P_{in}$) was similar to pressure seen by the circulation ($P_{ao} - P_{lv}$) at end diastole, there was quite a large difference between these values at end systole, especially under the higher pump flow conditions. Therefore, the control variable, that is, the average pressure difference between the left ventricle and the aorta, was different from the estimated pump differential pressure in our study.

Using a similar approach to Giridharan et al., Wu et al. (7) based their algorithms on the control of aortic pressure rather than pump differential pressure. A state space model of the human circulatory system as well as measurements of pump differential pressure was used to estimate the aortic pressure. The primary advantage of these algorithms was that it allowed for an automatic response to the changing metabolic demands of the circulatory system (22). However, it was shown from our results (Figs. 5 and 8) that maintaining pump differential pressure or aortic pressure at a constant value may increase the risk of suction under low SVR or V_{total} conditions while producing lower than optimal $\overline{CO}$ under higher V_{total} conditions. In particular, most CHF patients experience reduced ability in the regulation of SVR during an increase in cardiac demand due to varying levels of neurohormonal abnormalities and deterioration in the metabolic vasodilatation response (42,43). For example, the decreased muscle flow in a CHF patient is not only caused by enhanced vasoconstriction, but also caused by impaired metabolic vasodilation (possibly due to abnormal endothelium function). This significantly affects the outcome of the control algorithm, which requires that the natural regulatory mechanism functions adequately in response to a change in the metabolic demand (21). Although Wu et al. (7) attempted to overcome this limitation by deriving their reference aortic pressure using the measured pump differential pressure, it was difficult to determine the appropriate relationship between these two variables.

Study limitations

In the present model, we have not taken into account aspects of reflex control as well as autoregulatory systems due to their complexity. In order to represent various events such as exercise and postural changes, it is important to incorporate the above mechanisms into the software model. However, careful attention would have to be taken while modeling the autoregulatory and autonomic reflex mechanisms based on existing observations reported in the literature using normal subjects, as reports have shown that the autoregulatory and reflex response in a chronic heart failure patient may be significantly different from that of a healthy subject (44).

CONCLUSION

We have investigated the effect of alterations in the model parameter values, that is, cardiac contractility, SVR, and V_{total}, on the efficiency of rotary pump assistance, using an optimized dynamic heart–pump interaction model previously developed in our laboratory. Using our observations from both experimental and simulation results, we comparatively evaluated a number of previously proposed control parameters, including PI control, GPI control, constant average pressure difference control, and constant aortic pressure control. It was found that the previously proposed control strategies were not able to perform well under highly varying circulatory conditions which alter the amount of venous return to the heart. Among these, control algorithms which relied on LV filling pressure, for example, P_{la} control or PI control, appeared to be the most robust as they emulated the Frank–Starling mechanism of the heart. Ideally, P_{la} control provides the most promising form of control; however, this requires the implantation of an invasive pressure sensor in the left atrium. Noninvasively, PI control requires a suction detector to avoid the instability caused by the discontinuity in $PI(Q_p)$ at the suction onset. The heart–pump interaction model can be used as (i) a predictive tool for various studies, for example, response to exercise and postural changes;

(ii) a platform for the evaluation of robust physiological pump control algorithms; and (iii) a tool to study the correlation between physiological variables and noninvasive variables under various conditions.

REFERENCES

1. Park SJ, Tector A, Piccioni W, et al. Left ventricular assist devices as destination therapy: a new look at survival. *J Thorac Cardiovasc Surg* 2005;129:9–17.
2. Vollkron M, Schima H, Huber L, Benkowski R, Morello G, Wieselthaler G. Development of a reliable automatic speed control system for rotary blood pumps. *J Heart Lung Transplant* 2005;24:1878–85.
3. Mason DG, Hilton AK, Salamonsen RF. Reliable suction detection for patients with rotary blood pumps. *ASAIO J* 2008;54:359–66.
4. Korakianitis T, Shi Y. Numerical comparison of hemodynamics with atrium to aorta and ventricular apex to aorta VAD support. *ASAIO J* 2007;53:537–48.
5. Vollkron M, Schima H, Huber L, Wieselthaler G. Interaction of the cardiovascular system with an implanted rotary assist device: simulation study with a refined computer model. *Artif Organs* 2002;26:349–59.
6. Vandenberghe S, Segers P, Meyns B, Verdonck PR. Effect of rotary blood pump failure on left ventricular energetics assessed by mathematical modeling. *Artif Organs* 2002;26:1032–9.
7. Wu Y, Allaire PE, Tao G, Olsen D. Modeling, estimation, and control of human circulatory system with a left ventricular assist device. *IEEE Trans Control Syst Technol* 2007;15:754–67.
8. Liu Y, Allaire P, Wood H, Olsen D. Design and initial testing of a mock human circulatory loop for left ventricular assist device performance testing. *Artif Organs* 2005;29:341–5.
9. Pantalos GM, Koenig SC, Gillars KJ, Giridharan GA, Ewert DL. Characterization of an adult mock circulation for testing cardiac support devices. *ASAIO J* 2004;50:37–46.
10. Timms D, Hayne M, McNeil K, Galbraith A. A complete mock circulation loop for the evaluation of left, right, and biventricular assist devices. *Artif Organs* 2005;29:564–72.
11. McConnell PI, Del Rio CL, Kwiatkowski P, Farrar DJ, Sun BC. Assessment of cardiac function during axial-flow left ventricular assist device support using a left ventricular pressure-derived relationship: comparison with pre-load recruitable stroke work. *J Heart Lung Transplant* 2007;26:159–66.
12. Chiang BB, Pantalos GM, Cerrito P, et al. Treadmill exercise in calves implanted with the AbioCor replacement heart. *ASAIO J* 2003;49:589–93.
13. Goldstein AH, Monreal G, Kambara A, et al. Partial support with a centrifugal left ventricular assist device reduces myocardial oxygen consumption in chronic, ischemia heart failure. *J Card Fail* 2005;11:142–51.
14. Jaski BE, Kim J, Maly RS, Branch KR, et al. Effects of exercise during long-term support with a left ventricular assist device. *Circulation* 1997;95:2401–6.
15. Schima H, Vollkron M, Jantsch U, et al. First clinical experience with an automatic control system for rotary blood pumps during ergometry and right-heart catheterization. *J Heart Lung Transplant* 2006;25:167–73.
16. Wieselthaler GM, Schima H, Hiesmayr M, et al. First clinical experience with the DeBakey VAD continuous-axial-flow pump for bridge to transplantation. *Circulation* 2000;101:356–9.
17. Arndt A, Nusser P, Graichen K, Muller J, Lampe B. Physiological control of a rotary blood pump with selectable therapeutic options: control of pulsatility gradient. *Artif Organs* 2008;32:761–71.
18. Choi S, Antaki JF, Boston JR, Thomas D. A sensorless approach to control of a turbodynamic left ventricular assist system. *IEEE Trans Control Syst Technol* 2001;9:473–82.
19. Choi S, Boston JR, Antaki JF. Hemodynamic controller for left ventricular assist device based on pulsatility ratio. *Artif Organs* 2007;31:114–25.
20. Giridharan GA, Skliar M. Nonlinear controller for ventricular assist devices. *Artif Organs* 2002;26:980–4.
21. Giridharan GA, Skliar M. Control strategy for maintaining physiological perfusion with rotary blood pumps. *Artif Organs* 2003;27:639–48.
22. Giridharan GA, Skliar M. Physiological control of blood pumps using intrinsic pump parameters: a computer simulation study. *Artif Organs* 2006;30:301–7.
23. Lim E, Dokos S, Salamonsen RF, Rosenfeldt FL, Ayre PJ, Lovell NH. Numerical optimization studies of cardiovascular-rotary blood pump interaction. *Artif Organs* 2012;36:E110–24.
24. Lim E, Dokos S, Cloherty SL, et al. Parameter-optimized model of cardiovascular–rotary blood pump interactions. *IEEE Trans Biomed Eng* 2010;57:254–66.
25. Esmore D, Spratt P, Larbalestier R, et al. VentrAssist left ventricular assist device: clinical trial results and clinical development plan update. *Eur J Cardiothorac Surg* 2007;32:735–44.
26. Klingensmith ME, Chen LE, Glasgow SC, Melby SJ. *The Washington Manual of Surgery*. Philadelphia, PA: Wolters Kluwer Health/ Lippincott Williams & Wilkins, 2008.
27. Morley D, Litwak K, Ferber P, et al. Hemodynamic effects of partial ventricular support in chronic heart failure: results of simulation validated with in vivo data. *J Thorac Cardiovasc Surg* 2007;133:21–8.
28. Meyns B, Siess T, Nishimura Y, et al. Miniaturized implantable rotary blood pump in atrial-aortic position supports and unloads the failing heart. *Cardiovasc Surg* 1998;6:288–95.
29. Vandenberghe S, Nishida T, Segers P, Meyns B, Verdonck P. The impact of pump speed and inlet cannulation site on left ventricular unloading with a rotary blood pump. *Artif Organs* 2004;28:660–7.
30. Guyton AC, Hall JE. *Textbook of Medical Physiology*. Philadelphia, PA: W.B. Saunders Company, 1996.
31. Farrar DJ. Physiology of ventricular interactions during ventricular assistance. In: Goldstein DJ, Oz MC, eds. *Cardiac Assist Devices*. Armonck, NY: Futura Publishing Co., Inc., 2000;15–26.
32. Reesink K, Dekker A, van der Nagel T, et al. Physiologic-insensitive left ventricular assist predisposes right-sided circulatory failure: a pilot simulation and validation study. *Artif Organs* 2004;28:933–9.
33. Gravlee GP, Davis RF, Smtammers AH, Undgerleider RM. *Cardiopulmonary Bypass: Principles and Practice*. Philadelphia: Lippincott Williams & Wilkins, 2007.
34. Slaughter MS, Pagani FD, Rogers JG, et al. Clinical management of continuous-flow left ventricular assist devices in advanced heart failure. *J Heart Lung Transplant* 2010;29:S1–39.
35. Yuhki A, Hatoh E, Nogawa M, Miura M, Shimazaki Y, Takatani S. Detection of suction and regurgitation of the implantable centrifugal pump based on the motor current waveform analysis and its application to optimization of pump flow. *Artif Organs* 1999;23:532–7.
36. Figueroa MS, Peters JI. Congestive heart failure: diagnosis, pathophysiology, therapy, and implications for respiratory care. *Respir Care* 2006;51:403–12.
37. Reesink K, Dekker A, Van der Nagel T, et al. Suction due to left ventricular assist: implications for device control and management. *Artif Organs* 2007;31:542–9.
38. Boston JR, Simaan MA, Antaki JF, Yu YC, Choi S. Intelligent control design for heart assist devices. *Proceedings of the 1998 IEEE ISIC/CIRNISAS Joint Conference*, Gaithersburg, 1998.

39. Bullister E, Reich S, d'Entremont P, Silverman N, Sluetz J. A blood pressure sensor for long-term implantation. *Artif Organs* 2001;25:376–9.

40. Simons AP, Reesink KD, Lance MD, et al. Dynamic filling index: a novel parameter to monitor circulatory filling during minimized extracorporeal bypass. *Eur J Cardiothorac Surg* 2009;36:330–4.

41. Karantonis DM, Lovell NH, Ayre PJ, Mason DG, Cloherty SL. Identification and classification of physiologically significant pumping states in an implantable rotary blood pump. *Artif Organs* 2006;30:671–9.

42. Tsutomu M. Endothelium dysfunction in heart failure. *Tokyo Heart J* 2000;2:81–5.

43. Sinoway L, Minotti J, Musch T, et al. Enhanced metabolic vasodilation secondary to diuretic therapy in decompensated congestive heart failure secondary to coronary artery disease. *Am J Cardiol* 1987;60:107–11.

44. Eckberg DL, Sleight P, Folkow B. *Human Baroreflexes in Health and Disease*. Oxford, UK: Clarendon Press, 1992.